Available online at www.sciencedirect.com

ScienceDirect

Acta Materialia 83 (2015) 187–202

Acta MATERIALIA

www.elsevier.com/locate/actamat

Solute adsorption and entrapment during eutectic Si growth in A–Si-based alloys

J.H. Li,[a,*] M. Albu,[b] F. Hofer[b] and P. Schumacher[a,c]

[a]*Institute of Casting Research, University of Leoben, Leoben, Austria*
[b]*Institute for Electron Microscopy and Nanoanalysis, Graz University of Technology, Graz Center for Electron Microscopy, Graz, Austria*
[c]*Austrian Foundry Research Institute, Leoben, Austria*

Received 8 May 2014; revised 21 September 2014; accepted 21 September 2014

Abstract—The solute adsorption and/or segregation as well as the solute entrapment of Sr, Na and Yb atoms during eutectic Si growth in a series of high-purity Al–5 wt.% Si alloys was investigated by multi-scale microstructure characterization techniques, including high-resolution transmission electron microscopy and atomic-resolution scanning transmission electron microscopy. The adsorption of Sr atoms was directly observed along the $\langle 1\,1\,2\rangle_{Si}$ growth direction of Si and/or at the intersection of multiple Si twins, which can be used to interpret the poisoning of the twin plane re-entrant edge and impurity induced twinning modification mechanisms, respectively. In contrast, Yb shows a different mechanism compared to the adsorption of Sr atoms. No significant Yb-rich cluster was observed at the intersection of Si twins. However, considerable Yb-rich segregation lines were observed along the $\langle 1\,1\,2\rangle_{Si}$ direction, which can be attributed to the solute entrapment caused by a few Si twins through the natural twin plane re-entrant edge and growth mechanism. Active poisoning of the twin plane re-entrant edge and impurity induced twinning growth mechanisms cannot be observed due to the absence of Yb atoms within eutectic Si. Furthermore, the solute entrapment of modifying elements (X, Sr or Yb) together with Al and Si was proposed to interpret the formation of Al_2Si_2X phases or X-rich clusters within eutectic Si. Such types of Al_2Si_2X phases or X-rich clusters were further proposed to be an "artefact" caused by the solute entrapment during eutectic Si growth, rather than an active factor affecting the modification. The observed solute adsorption and entrapment can be used to interpret the different observations in the cases of different modifying elements, including impurity effects and so-called "quenching modification", thereby elucidating the modification of eutectic Si in Al–Si alloys.

Keywords: Al–Si alloy; Segregation; Adsorption; Solute entrapment; Eutectic solidification

1. Introduction

The modification of eutectic Si in Al–Si alloys can be dated back to 1921, when the first modification phenomenon was discovered by Pacz [1]. Recent technological developments of electron microscopy, e.g. high-resolution transmission electron microscopy (HRTEM), high-resolution scanning transmission electron microscopy (HRSTEM) and atom probe tomography (APT), make it possible to investigate the modification mechanisms at an atomic scale. To date, it is generally accepted that impurity induced twinning (IIT) [2] and the twin plane re-entrant edge (TPRE) growth mechanism [3,4], as well as poisoning of the TPRE [5], are valid under certain conditions. The IIT mechanism postulates that the impurities (i.e. Sr and Na atoms) can be adsorbed on the growing $\{1\,1\,1\}_{Si}$ planes, producing frequent multiple Si twins. The TPRE mechanism proposes that Si growth occurs more readily at the re-entrant edge along the $\langle 1\,1\,2\rangle_{Si}$ growth direction of Si, whereas poisoning of the TPRE assumes that the modifier retards Si growth by selectively adsorbing at the TPRE, thus deactivating the growth advantage of the TPRE and forcing new growth of the TPRE. However, IIT, TPRE or poisoning of the TPRE cannot be used to interpret all the previous modification observations. Three salient observations highlight the limitations of the existing proposed modification mechanisms.

Firstly, Yb addition into Al–Si alloys has been reported to only refine, rather than modify, the eutectic Si [6], even though the Yb atom has an exactly suitable radius ratio ($r_{Yb}/r_{Si} = 1.646$) according to the IIT mechanism. A similar investigation of the addition of rare earth elements (i.e. La, Ce, Pr, Nd, Sm, Gd, Tb, Dy, Ho, Er, Tm, Yb and Lu) has been also reported [7]. Only Eu was found to modify the eutectic Si to a fibrous morphology, while other remaining rare earth elements were found to solely refine the plate-like Si, although these rare earth elements have a similar radius ratio ($r/r_{Si} \sim 1.646$), which is expected to modify eutectic Si according to the IIT mechanism. The observed disagreements

* Corresponding author. Tel.: +43 3842 402 3304; fax: +43 3842 402 3302; e-mail: jie-hua.li@hotmail.com

http://dx.doi.org/10.1016/j.actamat.2014.09.040
1359-6462/

strongly indicate that the well-accepted IIT mechanism, based on the atomic radius alone, is not capable of explaining the modification of eutectic Si, and additional mechanisms are still expected to be active.

Secondly, according to the IIT and/or poisoning of the TPRE mechanisms, the presence or adsorption of a single Sr atom at the twin re-entrant edges (for poisoning of the TPRE) or at the intersection of Si twins (for IIT) can result in the formation of parallel (for poisoning of the TPRE) or multiple (for IIT) Si twins, and thereby a modification of eutectic Si. However, instead of a single Sr atom, the formation of an Al_2Si_2Sr phase or Sr-rich cluster (with high Sr contents) within eutectic Si was very often observed [8,9], which cannot be fully interpreted using IIT or poisoning of the TPRE mechanisms. There is thus a great need to revise the solute adsorption and entrapment of Sr atoms during the modification of eutectic Si, and thereby to elucidate this important melt treatment for Al–Si-based alloys.

Thirdly, the effect of cooling rates or growth rates on the formation of Si twins has not been fully considered in either IIT or poisoning of the TPRE mechanisms. It is well accepted that cooling rate (respectively undercooling) at the interface is one of the most important factors to affect the nucleation and growth of eutectic Si. Increasing cooling rates (i.e. melt-spinning) results in a so-called "quenching modification" [2,10]. It has been reported that only when the cooling rate is faster than the critical cooling rate, which is dependent on the diffusion coefficient of the modifier, can the modification of eutectic Si be achieved [11]. With further increasing of the undercooling (up to 350–400 K), as reported in Ref. [12], metallic liquids solidification can be so fast that the interface velocity (V) is of the order of, or even greater than, the diffusion speed (V_D) in the bulk liquid, having a high crystal growth velocity up to 100 m s^{-1}. In the case of such a deep undercooling, the approximation of local equilibrium may become unacceptable for the description of solute diffusion. More importantly, increasing cooling rates may change the modes of solute diffusion. The solid–liquid interface is no longer in equilibrium, and it is generally accepted, and has been demonstrated for solid solutions, that increasing cooling rates gives rise to a reduced partitioning, leading to a solid having the same composition as the liquid through a process known as "solute trapping" [13]. It has been also argued [14] that, when the solidifying phase shows a site ordering, the partitioning behaviour can be considerably more complex: rapid solidification might lead to an increased partitioning, a change in the direction of partitioning or an absence of partitioning at solidification rates much lower than expected. The experimental verification of this phenomenon has also been reported by demonstrating inverted partitioning during rapid solidification of the intermetallic compound NiAl [15]. Clearly, increasing cooling rates results in a significant change to the solute diffusion or partitioning behaviour. Furthermore, the solute diffusion or partitioning behaviour of impurities (i.e. Sr and Na) ahead of the solidification front of eutectic Si under higher cooling rates was believed to have a vital effect on the modification of eutectic Si. However, most previous work focuses on the Al–Si alloys produced by conventional casting, i.e. sand-casting or die-casting [2,8,16,17]. An investigation of the solute adsorption and entrapment during Si growth under higher cooling rates (i.e. melt-spun condition) is still required.

In this paper, the solute adsorption and entrapment during eutectic Si growth in a series of high-purity Al–5 wt.% Si alloys with Sr, Na and Yb additions were investigated, with a special focus on the distribution of Sr and Yb atoms within eutectic Si, in particular along the $\langle 1\,1\,2\rangle_{Si}$ growth direction of Si and/or at the intersection of multiple Si twins. Furthermore, the factors affecting the modification of eutectic Si were also discussed in terms of eutectic Si growth. For the first time, solute entrapment was proposed to interpret the different observations in the cases of different modifying elements under different cooling conditions.

2. Experimental material and procedures

A series of Al–5 wt.% Si alloys (wt.% is used through the paper where not specified otherwise) with the additions of Sr, Na and/or Yb were prepared using arc-melting and subsequent melt-spinning. The details on sample preparations (i.e. arc-melting and melt-spinning) are reported in Ref. [18]. The nominal composition is listed in Table 1. It is noteworthy that the Na content (50 ppm in Alloys 3 and 5) was added by Al–5Si–200 ppm Na master alloy manufactured by 5 N (99.998) Al, 5 N Si and 2 N (99.8) Na. Al–5Si–200 ppm Na master alloy was produced using conventional die-casting under an Ar protection. Due to the production method of Al–5Si–200 ppm Na master alloy, a low Fe level was observed. Sr and Yb additions were made by using Al–4Sr and Al–5Yb master alloys produced using arc-melting and by 5 N Al, 2 N Sr and 5 N Al, 2 N Yb, respectively. The Al–5Si–200 ppm Sr alloy (Alloy 6) was produced by conventional die-casting using 2N8 Al, 5NSi and commercial Al–10Sr master alloy, with the aim to elucidate whether the observation in high-purity melt-spun samples is valid at commercial purity samples produced by conventional die-casting.

The ribbons for the TEM investigation were mechanically ground, polished and dimpled to ~30 μm, and then ion-beam-milled using a Gatan Precision Ion Polishing System (PIPS, Gatan model 691). A constant preparation temperature (~−10 °C) was maintained by using a cold stage during ion beam polishing. Conventional TEM was performed using a Philips CM12 microscope operated at 120 kV. HRTEM micrographs and energy-dispersive X-ray spectroscopy (EDX) investigations were performed using a Cs-corrected JEOL-2100F microscope operated at 200 kV. The HRSTEM micrographs and EDX investigations were performed using a monochromated and probe-corrected FEI Titan^{3TM} G2 60–300 (S/TEM) microscope operated at 300 kV with an X-FEG high-brightness

Table 1. Nominal compositions of Al–5Si based alloys with Sr, Na and/or Yb additions (wt.%).

Alloy designation	Nominal alloy compositions
Alloy 1	Al–5Si
Alloy 2	Al–5Si–200 ppm Sr
Alloy 3	Al–5Si–50 ppm Na
Alloy 4	Al–5Si–6100 ppm Yb
Alloy 5	Al–5Si–50 ppm Na–6100 ppm Yb
Alloy 6	Al–5Si–200 ppm Sr

Note: Alloy 2 and Alloy 6 were produced by melt spinning and conventional die casting, respectively.

emission gun. The high-resolution images in STEM mode were recorded with a beam diameter of 0.1 nm and a current of 0.04 nA using the high-angle annular dark field (HAADF) and dark field (DF) detectors. X-ray spectra were acquired by the SuperX detection system (Chemi-STEM™ technology) with a 120 mm acquisition area which reduces significantly the acquisition times. Elemental quantification of the EDX spectra was performed using the Zeta factor method [19]. The images and spectra were recorded by a Gatan Digiscan unit and Digital Micrograph software, and were corrected for dark current and gain variations.

3. Results

3.1. Microstructure of melt-spun ribbons

3.1.1. Al–5Si alloy without addition

Fig. 1 shows a typical microstructure in high-purity melt-spun Al–5Si alloy. A Si particle located along the grain boundary is highlighted in Fig. 1a. Viewed from $\{0\,1\,1\}_{Si}$ zone axis (Fig. 1b), the Si particle appears to grow by the natural TPRE mechanism. The marked orientation (Fig. 1a) is fully consistent with that of TPRE, i.e. the

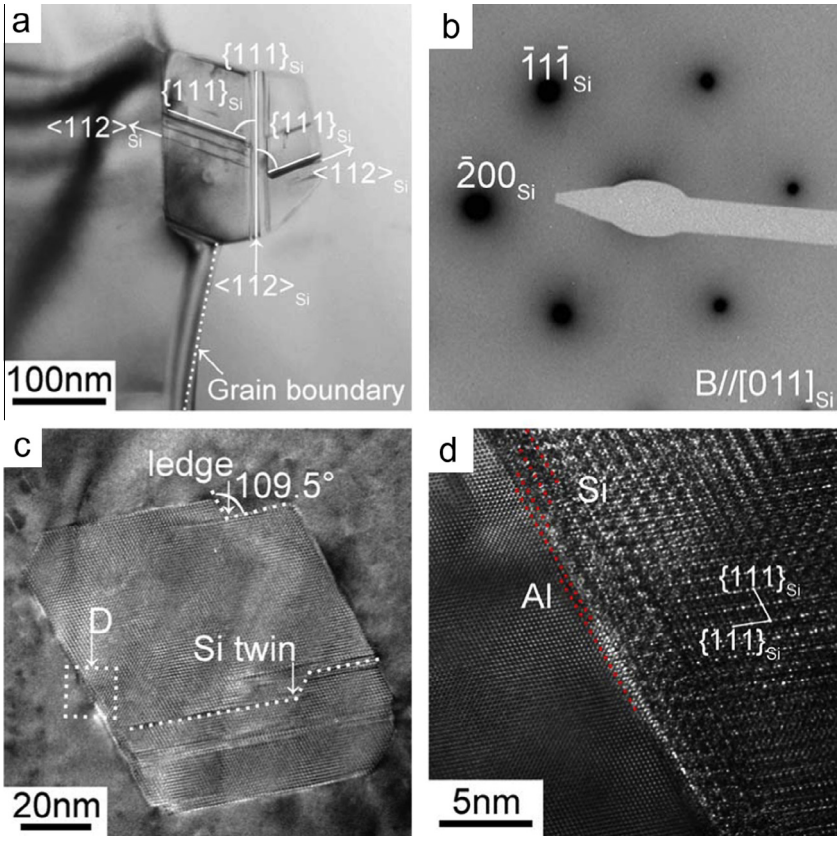

Fig. 1. (a) TEM bright-field image, (b) corresponding $[0\,1\,1]_{Si}$ SADP and (c, d) HRTEM images of Si particles, tilted to $[0\,1\,1]_{Si}$ zone axis, in high-purity melt-spun Al–5Si alloy.

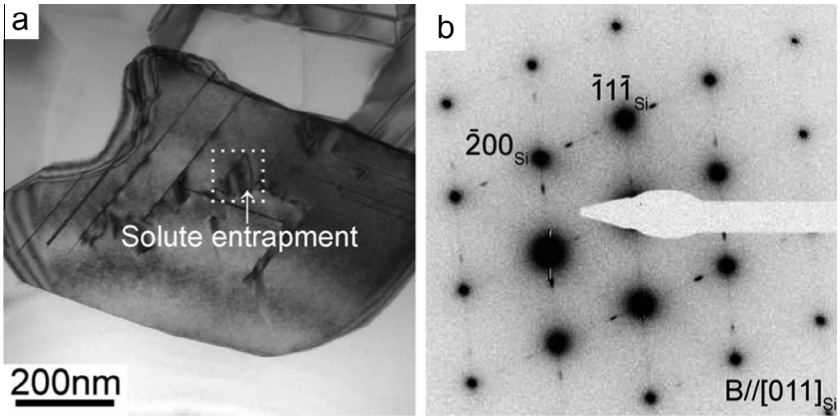

Fig. 2. (a) TEM bright-field image, (b) corresponding $[0\,1\,1]_{Si}$ SADP taken from high-purity melt-spun Al–5Si–200 ppm Sr alloy.

typical $\langle 1\,1\,2\rangle_{Si}$ growth direction. In order to further elucidate the details within eutectic Si, a HRTEM image is shown in Fig. 1c. Indeed, Si twinning was grown on one special plane (i.e. $\{1\,1\,1\}_{Si}$), rather than multiply twinned, as marked with a dashed white line in Fig. 1c. Some ledges were also observed, as marked with a white solid arrow in Fig. 1c. The position of the ledge is expected to be feasible for the adsorption of modifying elements, i.e. Sr and Na. Some steps were also observed at the interface between Si and Al, as marked with red dashed lines in an enlarged HRTEM image taken from the area as marked (D) with a white box in Fig. 1c, and highlighted in Fig. 1d. Such types of steps are located at the solidification front, and thereby can provide the positions for the possible adsorption of modifying elements.

3.1.2. Al–5Si alloy with Sr addition

The addition of Sr (up to 200 ppm) into high-purity melt-spun Al–5Si alloys promotes significant Si twinning during eutectic Si growth. In contrast to Fig. 1 (without Sr addition), most Si particles were multiply twinned. Fig. 2 shows a multiply twinned Si particle in high-purity melt-spun Al–5Si–200 ppm Sr alloy. Fig. 2b shows the selected area diffraction pattern (SADP) taken by tilting to the $\langle 0\,1\,1\rangle_{Si}$ zone axis with double diffractions of two variants. It should be noted that some particles appear to be entrapped by the formation of multiple Si twins, as marked with a white solid arrow in Fig. 2a.

In order to further elucidate the location and distribution of Sr within eutectic Si, Fig. 3a shows a low-magnification STEM-HAADF image of multiply twinned Si particles

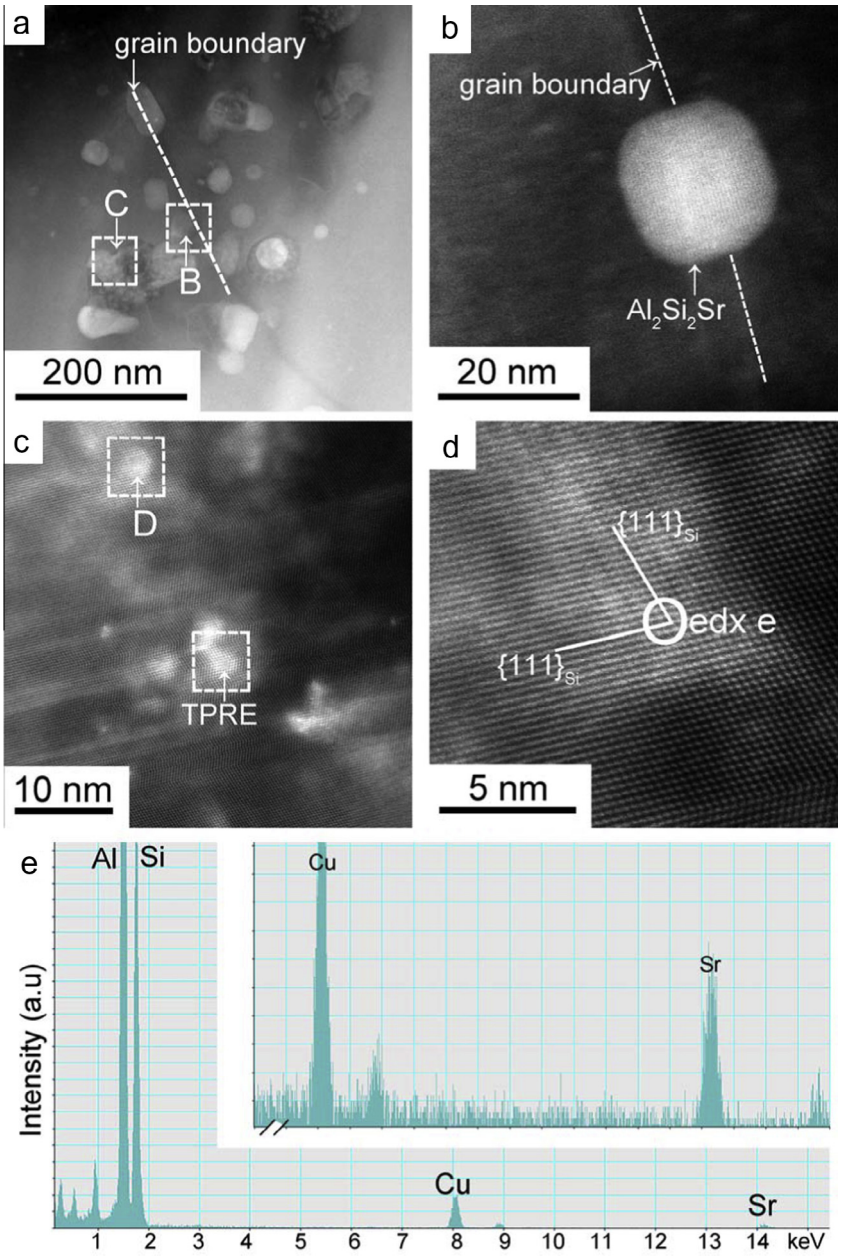

Fig. 3. (a) STEM-HAADF image taken from high-purity melt-spun Al–5Si–200 ppm Sr alloy, (b) is enlarged from the area marked with a white box (B) in (a), showing the Al_2Si_2Sr particle along the grain boundary, (c) is enlarged from the area marked with a white box (C) in (a), showing the Sr-rich clusters along the $\langle 1\,1\,2\rangle_{Si}$ growth direction of Si and at the intersection of Si twins, (d) is enlarged from the area marked with a white box (D) in (c), showing the Sr-rich cluster at the intersection of Si twins. (e) EDX analysis of the Sr-rich cluster, as marked in (d). B//$[0\,1\,1]_{Si}$.

and Al_2Si_2Sr particles in high-purity melt-spun Al–5Si–200 ppm Sr alloy. Fig. 3b is enlarged from one area marked (B) with a dashed line in Fig. 3a, showing an Al_2Si_2Sr particle at the grain boundary. The size of the Al_2Si_2Sr particle is ~20 nm. Due to its high disregistry between Si and Al_2Si_2Sr (Table 2), it is highly unlikely that the Al_2Si_2Sr intermetallic acts as nuclei for Si [8]. Fig. 3c is enlarged from the other area marked (C) with a dashed box in Fig. 3a, showing a multiply twinned Si particle. As expected from poisoning of the TPRE and IIT mechanisms, Al–Si–Sr-rich clusters were observed along the $\langle 1\,1\,2\rangle_{Si}$ growth direction of Si (Fig. 3c) and at the intersection of two $\{1\,1\,1\}_{Si}$ twins (marked D in Fig. 3c, and highlighted in Fig. 3d), respectively. A bright contrast in STEM-HAADF image corresponds to a higher Z (atom number) since the HAADF signal scales with Z^2 (Z_{Sr} is 38, much higher than Z_{Al} (13), Z_{Si} (14)). The EDX analysis (Fig. 3e) taken from the marked area in Fig. 3d indicates that Sr as well as Si and Al, thus Al–Si–Sr-rich clusters, rather than separate Sr atoms, form at the intersection of two $\{1\,1\,1\}_{Si}$ twins. It should be noted that some Al signals may also come from the matrix. The signal of Cu (at ~8 keV) is coming from the Cu ring supporting the TEM sample.

In order to elucidate the possible difference between melt-spun condition and the controlled cooling condition, the samples were also investigated after differential scanning calorimetry (DSC). After DSC (heating from 400 °C to 600 °C and subsequent cooling from 600 °C to 400 °C with a rate of 10 °C min^{-1}), the size of Si particles grows to ~5 μm (Fig. 4a), much larger than that (~250 nm, Fig. 2a) in the melt-spun condition. Interestingly, during such a slower cooling (similar to conventional die-casting, as for Alloy 6), multiple Si twins formed within eutectic Si. Al–Si–Sr-rich clusters were again observed along the $\langle 1\,1\,2\rangle_{Si}$ growth direction of Si and at the intersection of two $\{1\,1\,1\}_{Si}$ twins, respectively, which is very similar to Fig. 3c and d. It should be noted here that the Si particle was tilted to the $\langle 1\,1\,1\rangle_{Si}$ (Fig. 4b), rather than to the

Table 2. Crystallographic data for some selected phases.

No.	Phase	Crystal structure	Lattice parameter (nm)	Disregistry (δ) (%)
1	Al	Cubic	$a = 0.40491$	33.66 when $(Al)_S$
2	Si	Cubic	$a = 0.5421$	
3	Al_2Si_2Sr	Hexagonal	$a = 0.41872$, $c = 0.7427$	8.46 when $(Al_2Si_2Sr)_S$
4	Al_2Si_2Yb	Hexagonal	$a = 0.414482$, $c = 0.68927$	8.37 when $Al_2Si_2Yb)_S$

Note: To calculate the lattice disregistry with Si (diamond cubic), $(0\,0\,0\,1)[1\,1\,-2\,0]_{Al_2Si_2Sr,Al_2Si_2Yb}//(1\,1\,1)[0\,1\,1]_{Si}$ and $(1\,1\,1)[0\,1\,1]_{Al}//(1\,1\,1)[0\,1\,1]_{Si}$ is applied.

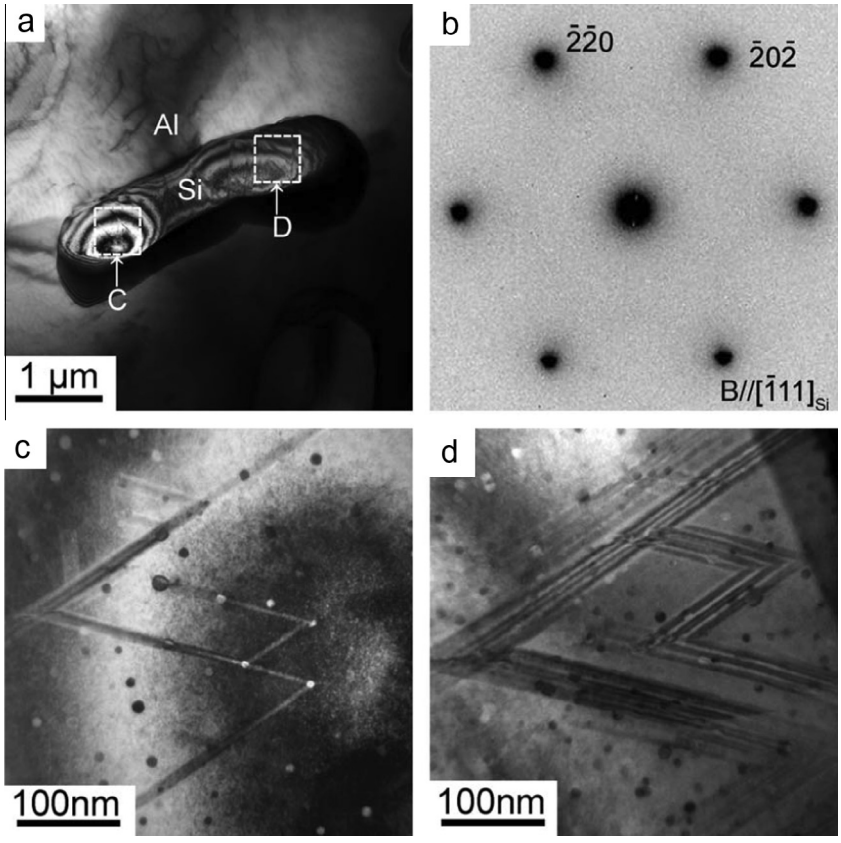

Fig. 4. (a) TEM bright-field image, (b) corresponding $[1\,1\,1]_{Si}$ SADP, (c, d) is enlarged from the areas marked with white boxes ((C) and (D)) in (a), showing the Sr-rich clusters along the $\langle 1\,1\,2\rangle_{Si}$ growth direction of Si and at the intersection of Si twins, taken from high-purity Al–5Si–200 ppm Sr alloy after DSC (heating from 400 °C to 600 °C and subsequent cooling from 600 °C to 400 °C with a rate of 10 °C min^{-1}).

$\langle 0\,1\,1\rangle_{Si}$ (Fig. 2b). Because of the fact that Si twins grow along the $\langle 1\,1\,2\rangle_{Si}$ growth direction on $\{1\,1\,1\}_{Si}$ growth planes, this orientation with the e-beam parallel to $\langle 1\,1\,1\rangle_{Si}$ makes it possible to observe the possible solute entrapment of modifying elements during eutectic Si growth, as discussed in Section 4.2. However, in this orientation $\langle 1\,1\,1\rangle_{Si}$, Si twins are not viewed edge-on, and therefore cannot appear very sharp when compared with Fig. 2a, viewed from $\langle 0\,1\,1\rangle_{Si}$. The zig-zag geometry was also clearly observed in Fig. 4c and d. Furthermore, this zig-zag geometry is different from that in the melt-spun condition, where Si twins grow along two $\langle 1\,1\,2\rangle_{Si}$ directions and on two different $\{1\,1\,1\}_{Si}$ planes (Fig. 2a). This difference can be attributed to the different cooling rates, as discussed in Section 4.3. It should be noted that the samples were not solidified under directional solidification conditions. Some decorations at corners along the $\langle 1\,1\,2\rangle_{Si}$ directions of Si growth were observed (Fig. 4c). These decorations are larger than those under melt-spun conditions (Fig. 3c and d). Large Al_2Si_2Sr particles with hexagonal close packed structure (Fig 5b and d) were also observed along the grain boundary, although their size increases from 20 nm (Fig. 3b) in the melt-spun condition up to 2 μm after DSC (Fig. 5a and c). Because of the larger size of the Si particles under slower cooling rates, more directions of Si growth can be observed.

3.1.3. Al–5Si alloy with Na addition

The addition of Na (up to 50 ppm) into high-purity melt-spun Al–5Si alloy promotes a significant increase of Si twins, as shown in Figs. 6 and 7. Similar to the addition of Sr (Figs. 2 and 3), after tilting to the principal twinning orientation of Si ($\langle 0\,1\,1\rangle$), significant multiple Si twins were observed, as shown in Fig. 6. Furthermore, the number density of Si twins (Figs. 6a and 7b) appears to be much higher than that in Al–5Si alloy without (Fig. 1a) or with (Fig. 2a) 200 ppm Sr addition. Fig. 7 shows parallel Si twins with a high twin density. In the vicinity of the Si particle, β-Al5FeSi phase was also observed by the segregation along grain boundaries. The parallel Si twins (Fig. 7b) and the multiple Si twins (Fig. 6c and d) with a high density can be attributed to poisoning of the TPRE mechanism and IIT mechanism, respectively. It should be noted that no attempt was made to take STEM-HAADF image and to elucidate the location and distribution of Na within eutectic Si, because of the fact that the atom numbers between Al, Si and Na are very close ($Z_{Na} = 11$, $Z_{Al} = 11$, $Z_{Si} = 14$). The brightness contrast of Na is considerably less strong than that of Sr ($Z_{Sr} = 38$). However, a similar behaviour, i.e. the adsorption of Na atoms along the $\langle 1\,1\,2\rangle_{Si}$ growth direction of Si (Fig. 7b) and at the intersection of two $\{1\,1\,1\}_{Si}$ twins (Fig. 6c and d), as well as the possible solute entrapment during eutectic Si growth (Fig. 6c and d), can be expected. A further careful observation shows that there is a ledge during eutectic Si growth, as marked with a white arrow and enlarged in Fig. 6d. At least two atom columns appear to be missing, which results in a change of stacking sequence, as marked with two white points in Fig. 6d. This observation is fully consistent with the IIT mechanism.

3.1.4. Al–5Si alloy with Yb addition

The addition of Yb (up to 6100 ppm) into high-purity melt-spun Al–5Si alloy has no significant effect on Si twinning, when compared to the additions of Sr (up to 200 ppm) (Fig. 2a) or Na (up to 50 ppm) (Figs. 6c and 7b). Fig. 8 shows a faceted Si particle tilted to the $\langle 0\,1\,1\rangle$

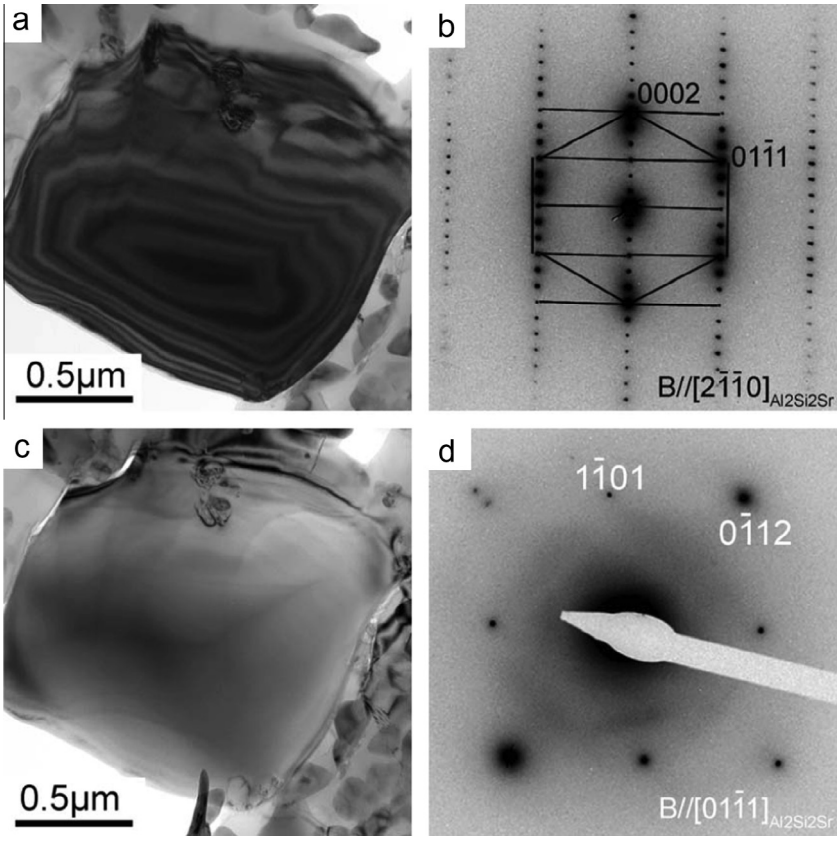

Fig. 5. (a, c) TEM bright-field images, (b, d) corresponding [2 1 1 0] and [0 1 1 1] SADPs, of an Al_2Si_2Sr phase, taken from high-purity Al–5Si–200 ppm Sr alloy after DSC (heating from 400 °C to 600 °C and subsequent cooling from 600 °C to 400 °C with a rate of 10 °C min^{-1}).

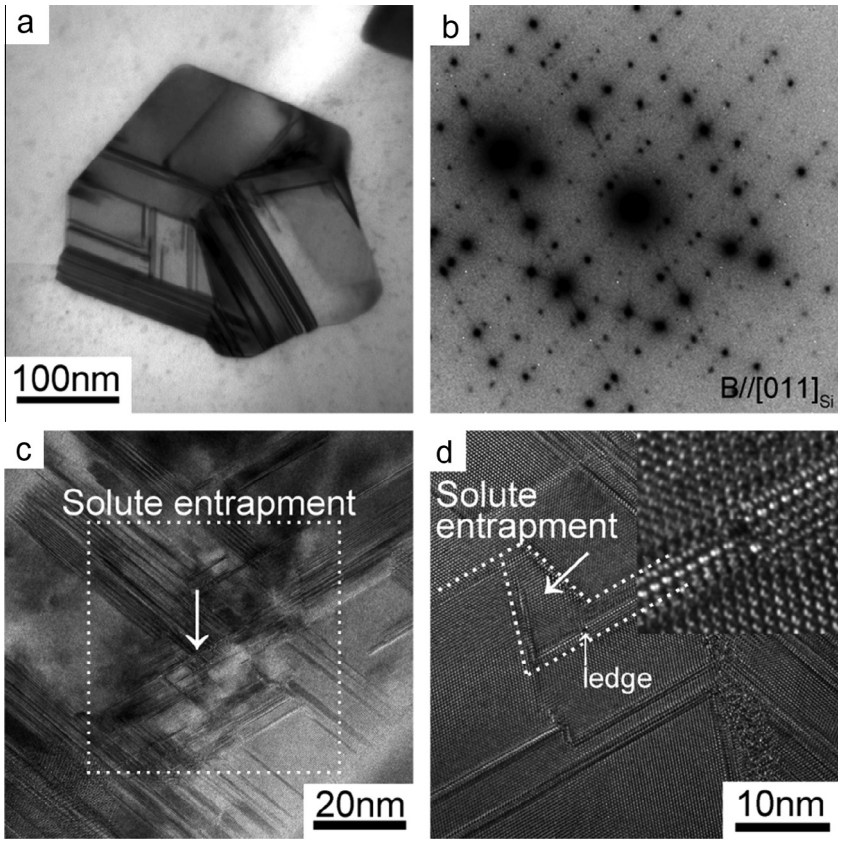

Fig. 6. (a) TEM bright-field image, (b) corresponding [0 1 1] SADP, (c) and (d) HRTEM images, of a Si particle taken from high-purity melt-spun Al–5Si–50 ppm Na alloy. The possible solute entrapment during Si growth was marked with a white box in (c). A ledge during Si growth was marked with a white arrow and enlarged in (d). At least two atom columns appear to be missing, which results in a change of stacking sequence, as marked with two white points in (d).

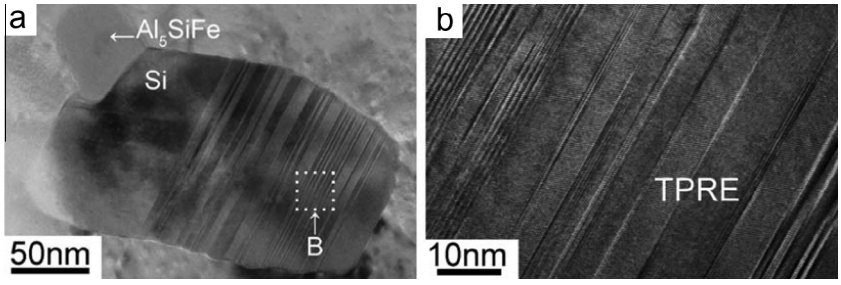

Fig. 7. (a) TEM bright-field image of a twinned Si particle in melt-spun Al–5Si–50 ppm Na alloy. (b) is enlarged from the areas marked with white boxes B) in (a), showing the parallel Si twinning. B//$[0\,1\,1]_{Si}$.

zone axis along the grain boundary in high-purity melt-spun Al–5Si–6100 ppm Yb alloy. Unexpectedly, no significant Si twinning was observed, even in the melt-spun condition, despite the favourable atom size ratio according IIT mechanism. A similar observation has also been reported in the conventional casting condition [6]. This observation is in contrast to the prediction of the IIT mechanism. Furthermore, no significant Yb-rich cluster was observed at the intersection of Si twins (Fig. 8b). However, when the sample was tilted away from $\langle 0\,1\,1\rangle_{Si}$ (Fig. 8c), considerable Yb-rich segregation lines were observed along the $\langle 1\,1\,2\rangle_{Si}$ direction (Fig. 8c) within the region marked (C) with a white dashed box in Fig. 8a. The Yb segregation can be further supported by the intensity (Fig. 8d) across the line marked (D) with a white dashed box in Fig. 8c. The thickness of the Yb segregation is about one or two atomic layers. Such types of Yb-rich segregation lines can be attributed to the solute entrapment during Si growth along $\langle 1\,1\,2\rangle_{Si}$ directions, as discussed in Section 4.2. Al_2Si_2Yb phase was also observed in the vicinity of the Si particle (Fig. 8a).

3.1.5. Al–5Si alloy with a combined Yb and Na addition

A combined addition of Na (up to 50 ppm) and Yb (up to 6100 ppm) into high-purity melt-spun Al–5Si alloy promotes a significant multiple Si twin, due to the presence of 50 ppm Na. Fig. 9a shows a low-magnification STEM-HAADF image of high-purity melt-spun Al–5Si–50 ppm Na–6100 ppm Yb alloy. Some isolated coarse Al_2Si_2Yb particles were observed within the α-Al matrix, as marked

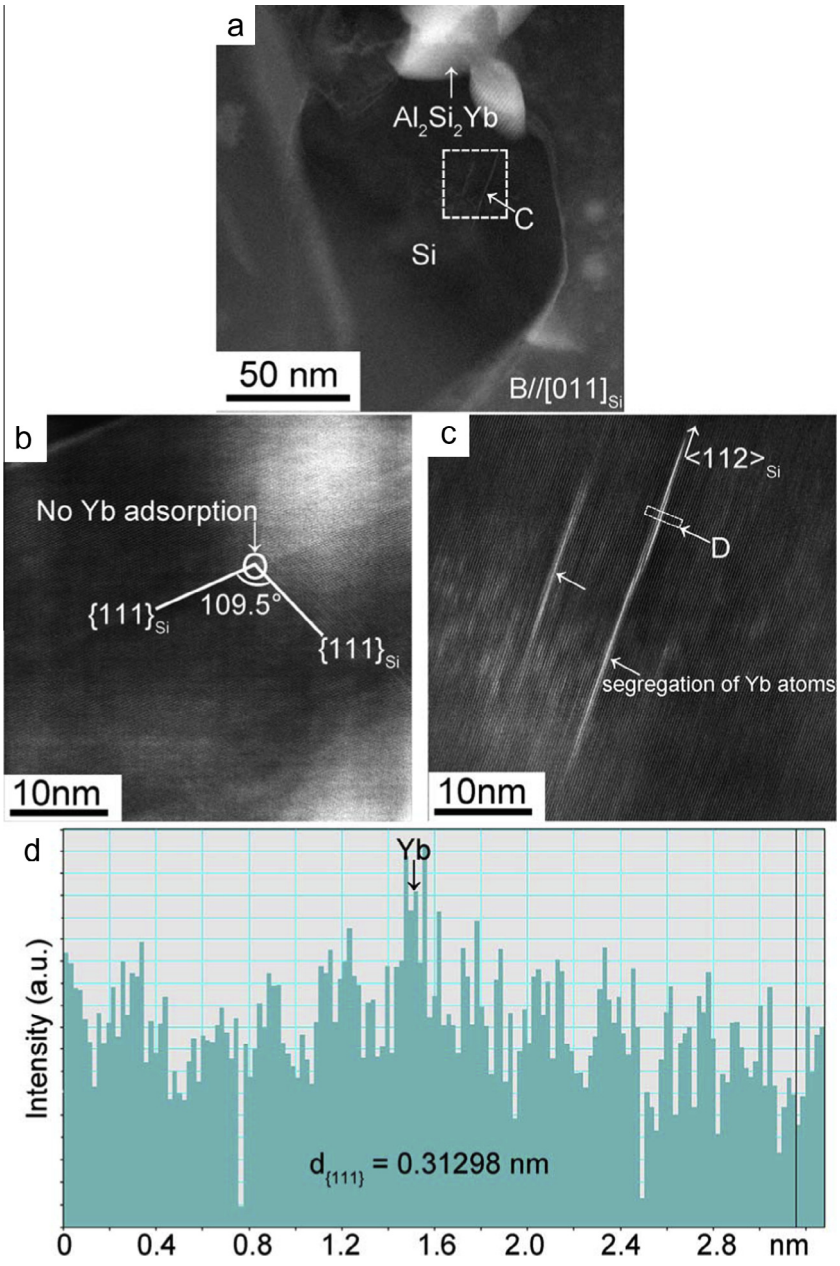

Fig. 8. (a) STEM-HAADF image taken from melt-spun Al–5Si–6100 ppm Yb alloy, (b) is enlarged from one area marked within a white box (C) in (a), showing no adsorption of Yb atoms at the intersection of Si twins, (c) is enlarged from another area marked within a white box (C) in (a), showing segregation lines of Yb atoms along the $\langle 1\,1\,2\rangle_{Si}$ growth direction of Si. (d) the intensity across the line marked with a white dashed box (D) in (c).

with a white arrow in Fig. 9a. Most Si particles are located along the grain boundaries. The size of these Si particles is very small, ~100 nm (Fig. 9c), indicating that the high Yb addition (6100 ppm) increases the undercooling of eutectic Si, thereby refining the eutectic Si. Fig. 9b is an enlarged area marked (B) with a white dashed box in Fig. 9a, showing finer Al_2Si_2Yb particles (~50 nm) at the grain boundary together with the eutectic Si and eutectic Al. Fig. 9c is an enlarged area marked (C) with a white dashed box in Fig. 9b, showing a multiply twinned Si particle. In contrast to the single addition of 6100 ppm Yb (Fig. 8), no significant Yb-rich segregation line was observed. However, Yb-rich clusters were observed at the intersection of Si twins (Fig. 9d). A weak Yb peak was observed using EDX analysis (Fig. 9e). The Yb enrichment can be attributed to (i) the solute entrapment during eutectic Si growth and (ii) the interaction between Na adsorption and Yb segregation. Further details will be discussed in Section 4.2.

3.2. Microstructure after conventional die-casting with a moderate cooling

In order to further elucidate whether the observation in high-purity melt-spun conditions is valid at conventional casting, the as-cast microstructure after conventional die-casting was also investigated. Similar to different observations between the Sr/Na addition and Yb addition in high-purity melt-spun Al–5Si alloys, it has been also reported that Na and Sr addition modified the eutectic Si to a fibrous morphology [7,8,11], while Yb addition just

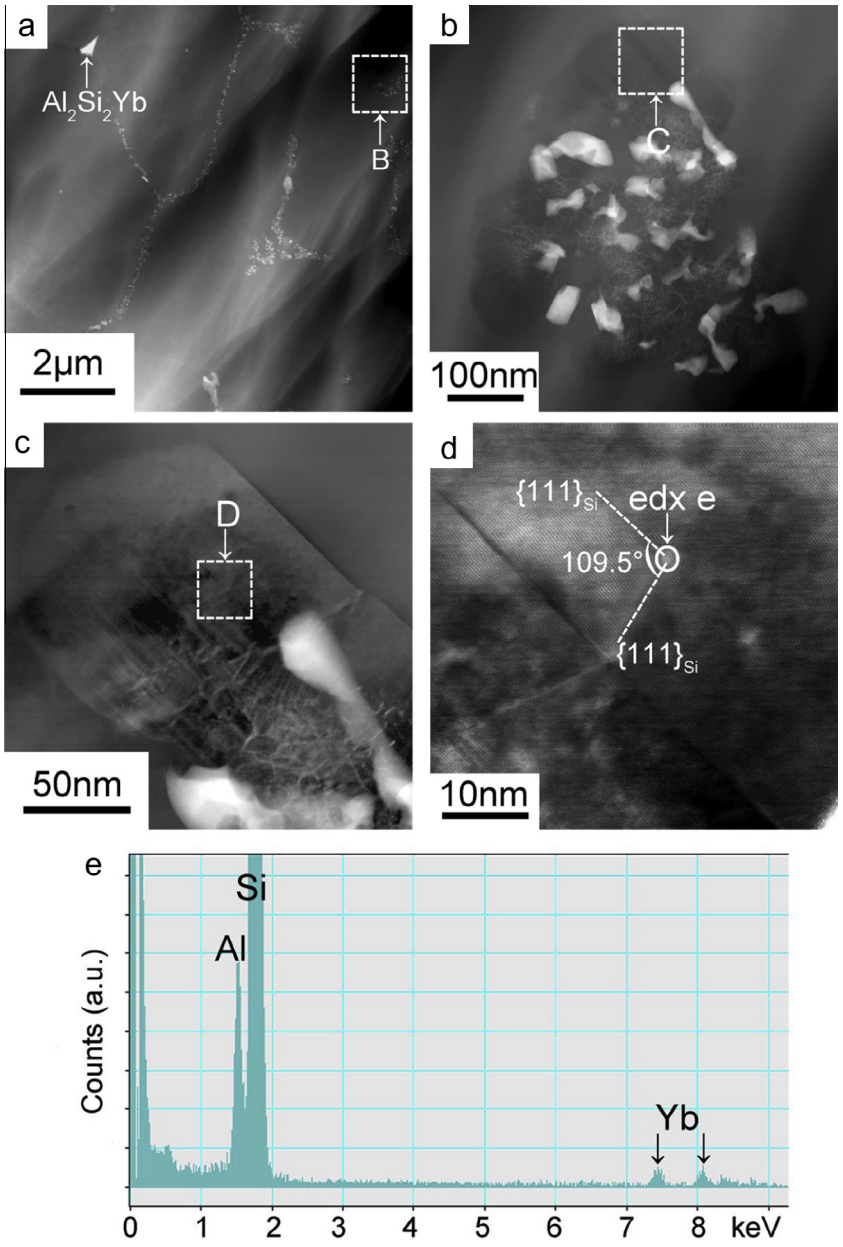

Fig. 9. (a) STEM-HAADF image taken from melt-spun Al–5Si–50 ppm Na–6100 ppm Yb alloy, (b) is enlarged from the area marked with a white box (B) in (a, c) is enlarged from the area marked with a white box (C) in (b), and (d) is enlarged from the area marked with a white box (D) in (c), showing no significant Yb adsorption along the $\langle 1\,1\,2\rangle_{Si}$ growth direction of Si and at the intersection of Si twins, although a week Yb peak was observed using EDX analysis (e).

refines the plate-like eutectic Si [6] after conventional casting. Thus, only results for Sr addition are shown here.

Fig. 10 shows a low-magnification STEM-HAADF image of commercial purity Al–5Si alloy with 200 ppm Sr addition produced by conventional die-casting (4 K s^{-1}). Fig. 10b is enlarged from the area marked (B) with a white dashed box in Fig. 10a, showing Al–Si–Sr-rich particles within eutectic Si, as marked with a white arrow in Fig. 10b. The Si growth directions and the Si growth planes are marked on the Al–Si–Sr-rich particles in Fig. 10b. EDX analysis (Fig. 10c) clearly shows that the Al–Si–Sr-rich particles have a chemical composition close to Al_2Si_2Sr phase. However, it should be noted that the formation of the Al_2Si_2Sr particles within eutectic Si is different from the formation of Al_2Si_2Sr particles at the grain boundaries directly from the liquid during solidification (Figs. 3b and 5). It can be attributed to the solute entrapment. Further details will be discussed in Section 4.2.

Fig. 11a and b is also enlarged from the area marked (B) with a white dashed box in Fig. 10a, showing the adsorption of Sr atoms at the intersection of Si twins. The adsorption of Sr atoms at the intersection of Si twins can be further supported by the intensity (Fig. 11c) across the line marked with a white dashed box in Fig. 11b.

In Fig. 12, another area in the same Si particle of Fig. 10, marked (B) with a white dashed box in Fig. 12a, was enlarged in Fig. 12b–d. The adsorption of Sr was observed along the $\langle 1\,1\,2\rangle_{Si}$ growth direction of Si. The adsorption of Sr along the $\langle 1\,1\,2\rangle_{Si}$ growth direction of Si can be further supported with the higher intensities in

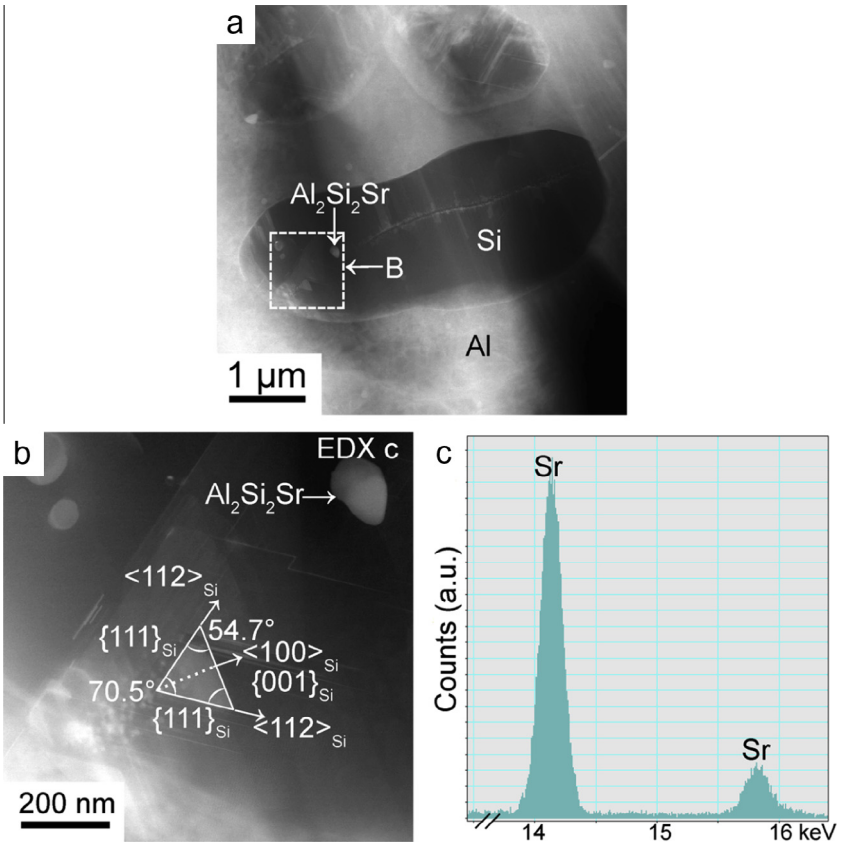

Fig. 10. (a) STEM-HAADF image taken from Al–5Si–200 ppm Sr alloy produced by conventional die-casting, (b) is enlarged from the area marked with a white box (B) in (a), showing the Al_2Si_2Sr particle within eutectic Si, (c) EDX analysis of the Al_2Si_2Sr particle, as marked in (b).

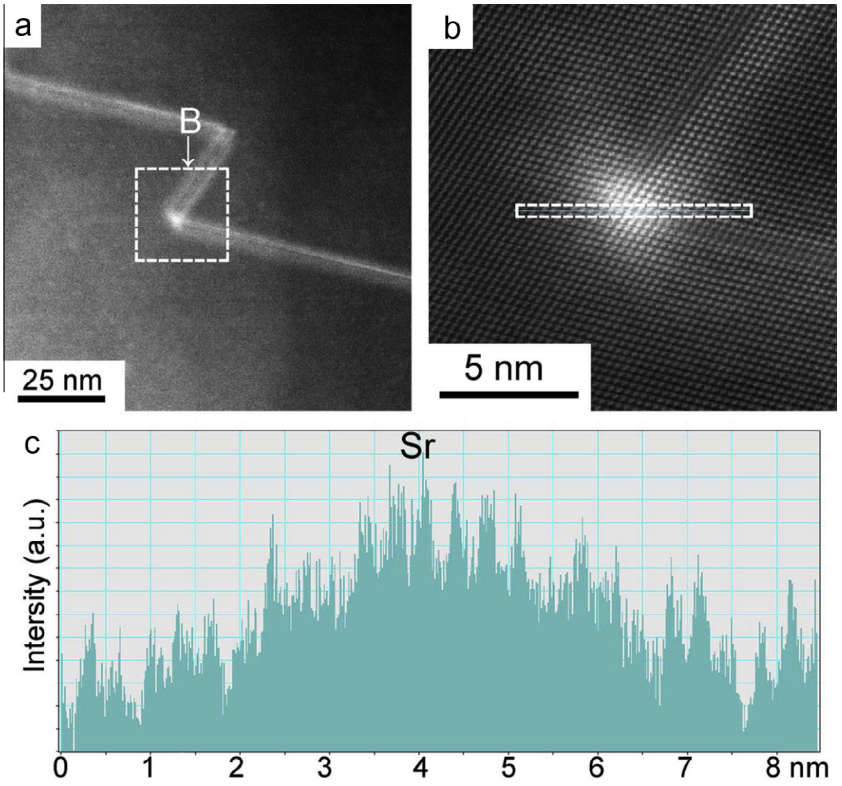

Fig. 11. (a) is enlarged from the area marked with a white box (B) in Fig. 10a, (b) is enlarged from the area marked with a white box (B) in (a), showing the Sr-rich clusters at the intersection of Si twins, (c) the intensity across the line marked with a white dashed box in (b).

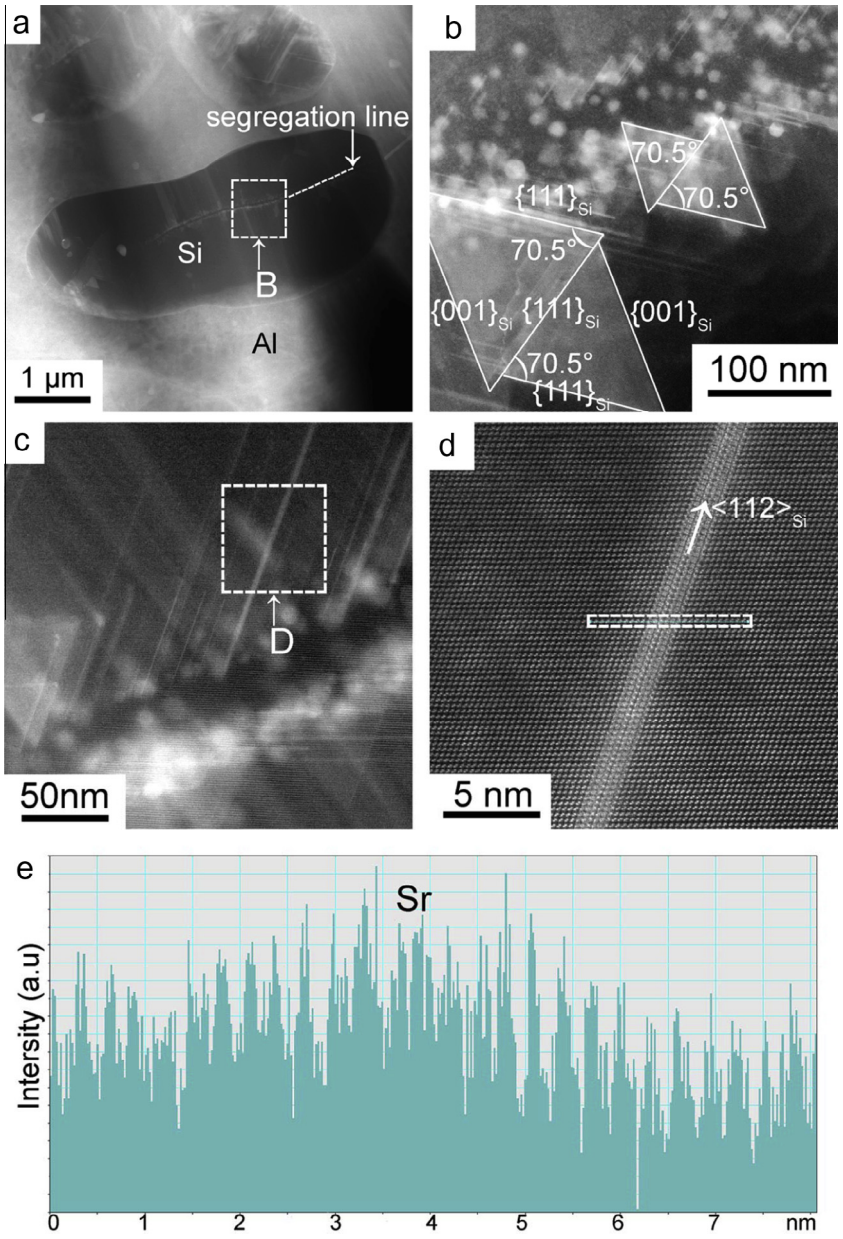

Fig. 12. (a) STEM-HAADF image taken from Al–5Si–200 ppm Sr alloy produced by conventional die-casting, (b) is enlarged from one area marked with a white box (B) in (a), (c) is enlarged from another area marked with a white box (B) in (a), (d) is enlarged from the area marked with a white box (D) in (c), showing the adsorption of Sr atoms along the $\langle 1\,1\,2\rangle_{Si}$ growth direction of Si. (e) the intensity across the line marked with a white dashed box in (d).

STEM images (Fig. 12e), which is plotted across the area marked with a white dashed box in Fig. 12d. Al–Si–Sr-rich particles (most likely Al_2Si_2Sr phase) were again observed within eutectic Si, as marked in Fig. 12b. The orientation in conventional casting is fully consistent with the observation in melt-spun conditions (Fig. 2a). In addition, an Al–Si–Sr-rich "band" was also observed along the $\langle 1\,1\,2\rangle_{Si}$ growth direction, as marked with a white dashed line in Fig. 12a. It can be attributed to the poisoning of the TPRE during eutectic Si growth.

4. Discussion

The addition of Sr (Figs. 2–4 and 10–12) and Na (Figs. 6 and 7) promotes a significantly multiply twinned Si, while the addition of Yb (Figs. 8 and 9) does not promote such a type of multiple Si twins despite its favourable atom size according to the IIT mechanism. Thus, the following discussions are separated in two different cases, with a special focus on the solute adsorption and/or segregation as well as the solute entrapment during eutectic Si growth. Heterogeneous nucleation of eutectic Si and undercooling in Al–Si alloys has been discussed elsewhere [9].

4.1. Sr or Na addition

The discussion will mainly focus on the Sr addition, due to a lack of a direct observation of Na atoms in STEM-HAADF images. However, it should be pointed out that a similar behaviour can be expected between Sr and Na on the basis of our above observations (Figs. 2, 3, 6 and 7) and previous reports [20–23]. The adsorption of Na on

$\{1\,1\,1\}_{Si}$ in Al–22 wt.% Si alloys with 0.25 and 0.6 wt.% Na additions has been reported using X-ray photoelectron spectroscopy and Auger electron spectroscopy [20,21]. The existence of Na-enriched regions within a spherical primary Si crystal has also been reported in Al–16 wt.% Si alloy with Na addition using electron probe microanalysis (EPMA) and back-scattered electron images [22]. Na-enriched regions were observed in narrow regions which spread wider from the centre to the periphery of the spherical Si. Furthermore, the Na atoms on the $\{1\,1\,1\}_{Si}$ surface have also been reported to be highly mobile around the Si rest atoms, forming a two-dimensional gas phase at the initial coverage, and at the higher coverage Na clusters emerge and form a self-assembled array, consisting of six Na atoms together with three Si atoms [23]. More recently, the adsorption of Na atoms at the intersection of multiple Si twins and along the $\langle 1\,1\,2\rangle_{Si}$ growth direction of Si as well as at the interface between eutectic Si and eutectic Al has been clearly observed using APT, which can provide a strong experimental support to IIT and poisoning of the TPRE mechanisms, respectively, in the case of Na addition [24]. For clarity, Fig. 13 shows a schematic representation of the Sr solute adsorption and/or segregation as well as the possible solute entrapment ahead of solidification front of eutectic Si in Al–Si alloys. Here, it should be pointed out that segregation is different from absorption. The former (segregation) will segregate out of eutectic Si, while the latter (adsorption) will remain at the interface and subsequently within eutectic Si during eutectic Si overgrowth. A combined effect of segregation and adsorption can result in the solute entrapment.

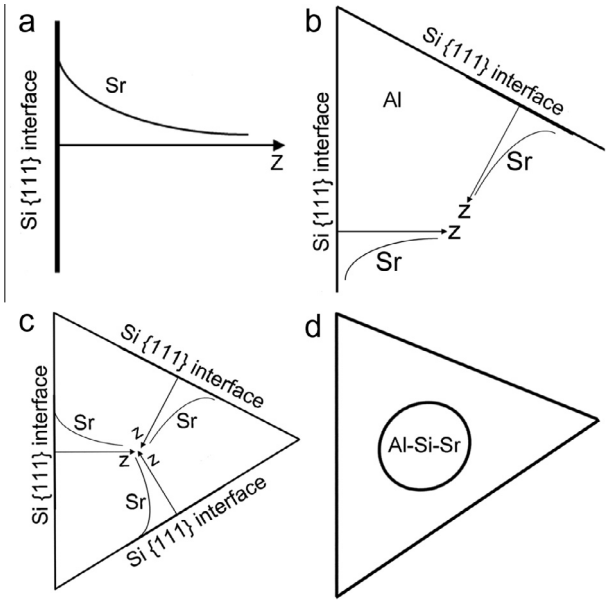

Fig. 13. Schematic representation of the adsorption of Sr atoms along the $\langle 1\,1\,2\rangle_{Si}$ growth direction of Si and at the intersection of Si twins, forming Si twinning, and the solute entrapment of Sr atoms, forming an Al_2Si_2Sr particle within eutectic Si. (a) Equilibrium solidification, (b) the adsorption of Sr atoms occurs along the $\langle 1\,1\,2\rangle_{Si}$ growth direction of Si and at the intersection of Si twins, forming Si twinning, (c) Sr adsorption occurs along other $\langle 1\,1\,2\rangle_{Si}$ growth direction of Si and at other intersection of Si twins, forming parallel or multiply Si twinning, (d) Sr solute entrapment occurs, forming Sr-rich clusters, finally Al_2Si_2Sr particle within eutectic Si.

In the liquid state, the alloying elements (i.e. Al, Sr and Si) are randomly distributed, although solute clustering (i.e. Si clustering) may occur [25]. During eutectic Si growth (Fig. 13a), Sr and Al solute will segregate ahead of the solidification interface ($k_{Al} < 1$ and $k_{Sr} < 1$). A solute redistribution of Sr and Al, and thus an enrichment of Sr and Al ahead of the solidification front, may occur. During continuous Si growth, the adsorption of Sr atoms on the $\{1\,1\,1\}_{Si}$ plane occurs along the $\langle 1\,1\,2\rangle_{Si}$ growth direction of Si and/or at the intersection of two $\{1\,1\,1\}_{Si}$ twins (Fig. 13b). According to the poisoning of the TPRE, the adsorption of Sr along the $\langle 1\,1\,2\rangle_{Si}$ growth direction of Si promotes the formation of further parallel Si twins with a higher number density. According to the IIT mechanisms, the adsorption of Sr at the intersection of two $\{1\,1\,1\}_{Si}$ twins promotes the formation of multiple Si twins.

The adsorption of Sr atoms at the intersection of Si twins and/or along the $\langle 1\,1\,2\rangle_{Si}$ growth direction can also occur during further eutectic Si growth, which may also yield further re-entrant edges of Si twinning or a change of stacking sequence of Si twinning (Fig. 13c). In this case, eutectic Si growth will re-start from another $\{1\,1\,1\}_{Si}$ plane. Similarly, an enrichment of Sr and Al atoms in a local area and another multiple Si twinning occurs. Finally, once the $\{1\,1\,1\}_{Si}$ planes fold on each other, the solute impingement and subsequent entrapment of the segregation fields occurs (Fig. 13d). On subsequent cooling, the solute entrapment forms Al–Si–Sr-rich particles with different morphologies and compositions, which are mostly likely to be Al_2Si_2Sr phase if the cooling rate is low enough, or the segregation time and length are sufficient.

It should be pointed out that the solute entrapment is different from the solute trapping [14,15]. Solute entrapment can be caused by the solute segregation of overlapping eutectic Si growth fronts, whereas solute trapping freezes the solutes from liquid states, and can only occur at an extremely high cooling rate (i.e. laser remelting). No complete solute trapping was observed in the present investigation, even under melt-spun conditions, indicating that the cooling rates and/or undercooling is still not significantly high enough to trap the solutes, and thereby result in a chemically partitionless (diffusionless) process. Thus, solute trapping was not taken further into consideration here.

The proposed solute entrapment can be used readily to interpret the observation of the Al–Si–Sr-rich clusters in the present investigation and previous reports using APT [8]. The observed Al–Si–Sr-rich clusters can be an "artefact" caused by solute entrapment, rather than an active factor affecting the modification. However, the observed Al–Si–Sr-rich clusters exhibit the position of the solute adsorption and subsequent entrapment during eutectic Si growth, i.e. along the $\langle 1\,1\,2\rangle_{Si}$ growth direction of Si and/or at the intersection of two $\{1\,1\,1\}_{Si}$ twins. Therefore, it is proposed that the adsorption of Sr is a dominant factor for modification of eutectic Si in Al–Si alloys, which leads to roughening and the formation of extended pits and regrowth structure, and thus a multiple Si twinning [23]. However, the observed Al–Si–Sr-rich clusters with different sizes and compositions are caused by the solute segregation and thereby the solute entrapment of Sr atoms, which were formed during eutectic Si growth, rather than the first and dominant step to lead to poisoning of the TPRE and IIT growth mechanisms.

4.2. Yb addition

In contrast to the cases of Sr and/or Na additions, no significant multiple Si twins were observed in the case of Yb addition. Only a refinement, rather than a modification, of eutectic Si was reported [6]. For clarity, Fig. 14 also shows a schematic representation of the solute segregation and subsequent entrapment of Yb atoms within eutectic Si in Al–Si alloys. Similar to the case of Sr addition (Fig. 13), in the liquid state, the alloying elements (i.e. Al, Yb and Si) are randomly distributed (Fig. 14a). During eutectic Si growth, Yb and Al segregation fields will impinge and segregate out ahead of the solidification front ($k_{Al} < 1$ and $k_{Yb} < 1$). A solute redistribution of Yb and Al, and thereby an enrichment of Yb and Al, may occur. However, in contrast to Sr addition, the adsorption of Yb atoms does not appear to occur on $\{1\,1\,1\}_{Si}$ planes during continuous eutectic Si growth (Fig. 8b). Instead, Yb atoms mostly segregate out and are only present along the $\langle 1\,1\,2\rangle_{Si}$ growth direction without causing further poisoning of the TPRE. This hypothesis can be strongly supported with our observation (Fig. 8c) and the previous report [17] that Yb is present just adjacent to the Si particle. Active poisoning of the TPRE and IIT mechanisms cannot be observed because insufficient Yb atoms remain along the $\langle 1\,1\,2\rangle_{Si}$ growth direction of Si and at the intersection of $\{1\,1\,1\}_{Si}$ twins. With continuous eutectic Si growth, the solute entrapment (Fig. 14b and c) may occur along the $\langle 1\,1\,2\rangle_{Si}$ growth direction of fewer Si twins, depending on the growth rate and local solute redistribution, which can be attributed to the natural TPRE mechanism as observed in Fig. 1a and by Wanger [2] and Hamilton and Seidensticker [3]. If such a type of solute segregation occurs, more and more Yb atoms will be segregated, forming a solute entrapment line (Fig. 14c), as

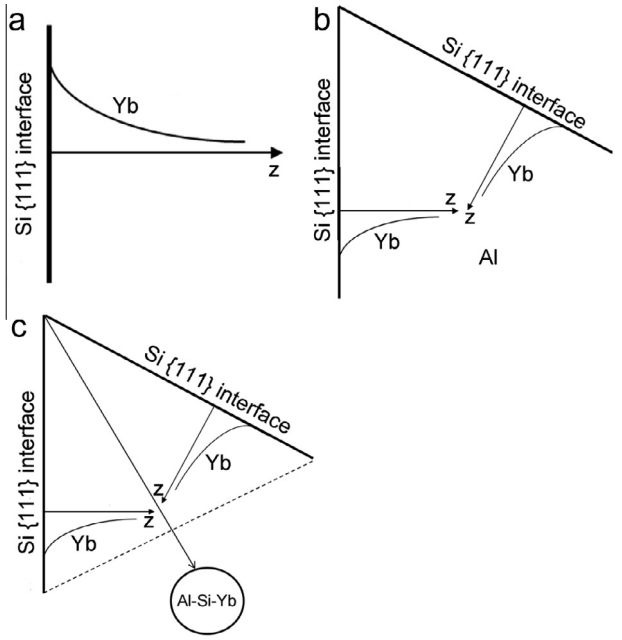

Fig. 14. Schematic representation of the segregation of Yb atoms along the $\langle 1\,1\,2\rangle_{Si}$ growth direction of Si, and the solute entrapment of Yb atoms, forming the Yb-rich segregation lines. (a) Equilibrium solidification, (b) The solute entrainment of Yb atoms occurs along the $\langle 1\,1\,2\rangle_{Si}$ growth direction of Si, (c) More Yb atoms are entrapped, forming Yb-rich segregation lines, and finally forming Al_2Si_2Yb phase in the vicinity of eutectic Si.

observed in Fig. 8c. However, it should be pointed out that although Yb-rich segregation lines form, no significant effect on the Si twinning can be expected because only an insufficient number of Yb atoms remain within eutectic Si and no poisoning of the TPRE occurs. Because of the absence of Yb atoms along the $\langle 1\,1\,2\rangle_{Si}$ growth direction of Si and at the intersection of two $\{1\,1\,1\}_{Si}$ twins, Yb addition (up to 6100 ppm) appears not to promote the formation of the parallel or multiple Si twinning (Fig. 8c). If any, only single Si twinning can be observed, which is similar to the case of Al–5Si-based alloy caused by natural TPRE (Fig. 1c). Furthermore, no Al_2Si_2Yb particle was observed within eutectic Si because no significant solute adsorption and/or entrapment of Yb atoms occurs during eutectic Si growth. Instead, most Al_2Si_2Yb particles were observed adjacent to the Si phase (Fig. 14c), strongly indicating that most Yb atoms segregate out of eutectic Si.

4.3. Diffusion behaviour ahead of the eutectic Si growth front

In the case of Sr addition, a consistent observation, i.e. the formation of multiple Si twins, was obtained in melt-spun conditions and conventional die-casting; however, the effects of the different cooling rates on the diffusion behaviour (i.e. diffusion length and the interfacial energy) ahead of the eutectic Si growth front should also be taken into consideration.

For clarity, Fig. 15 shows a schematic representation to elucidate the diffusion behaviour ahead of the eutectic Si growth front and its effects on the formation of the parallel Si twinning caused by TPRE (Fig. 15a) or poisoning of the TPRE (Fig. 15c and d) and the multiple Si twinning caused by IIT (Fig. 15e and f), as marked in Fig. 15b. In the case of TPRE, the Si grows along the $\langle 1\,1\,2\rangle_{Si}$ growth direction. No further Si twins can be induced due to a lack of the adsorption of Sr atoms along TPRE (Fig. 15a). In the case of poisoning of the TPRE, the adsorption of Sr atoms occurs along the $\langle 1\,1\,2\rangle_{Si}$ growth direction of Si, as shown in Fig. 15c. Similarly, the same adsorption of Sr atoms also occurs on other $\{1\,1\,1\}_{Si}$ growth planes along the $\langle 1\,1\,2\rangle_{Si}$ growth direction of Si, as shown in Fig. 15d. Further Si twins can be induced, as shown in Fig. 15b. The diffusion space (λ) is marked in Fig. 15d. In the case of IIT, the adsorption of Sr atoms occurs at the intersection of two $\{1\,1\,1\}_{Si}$ twins, as shown in Fig. 15e. Similarly, the adsorption of Sr atoms also occurs at the intersection of two $\{1\,1\,1\}_{Si}$ twins on other $\{1\,1\,1\}_{Si}$ growth planes, as shown in Fig. 15f. The diffusion space (λ) is also marked in Fig. 15f.

It should be noted here that the diffusion behaviour of Sr atoms ahead of the eutectic Si growth front is very similar to that of binary eutectic during eutectic solidification (i.e. $L \rightarrow \alpha + \beta$) [26]. Therefore, the diffusion space (λ) (Fig. 15b, d and f) can be related to the lamellar spacing (λ^*) during eutectic solidification (in the case of lamellar eutectic). The main difference is that the diffusion space between Si twins is defined within eutectic Si, while the lamellar spacing is defined within two different eutectic phases (α, β).

Similar to the lamellar spacing (λ^*) during eutectic solidification, diffusion space (λ) can be determined by the interface energies, diffusion rates in the melt, volume fraction of the Si twins, preferred orientation for growth and relative growth rates of the Si twins. In the case of melt-spinning, the preferred orientation for growth and relative growth rates of Si twins can be expected to remain unchanged. However, the adsorption of the modifying elements (Sr, Na)

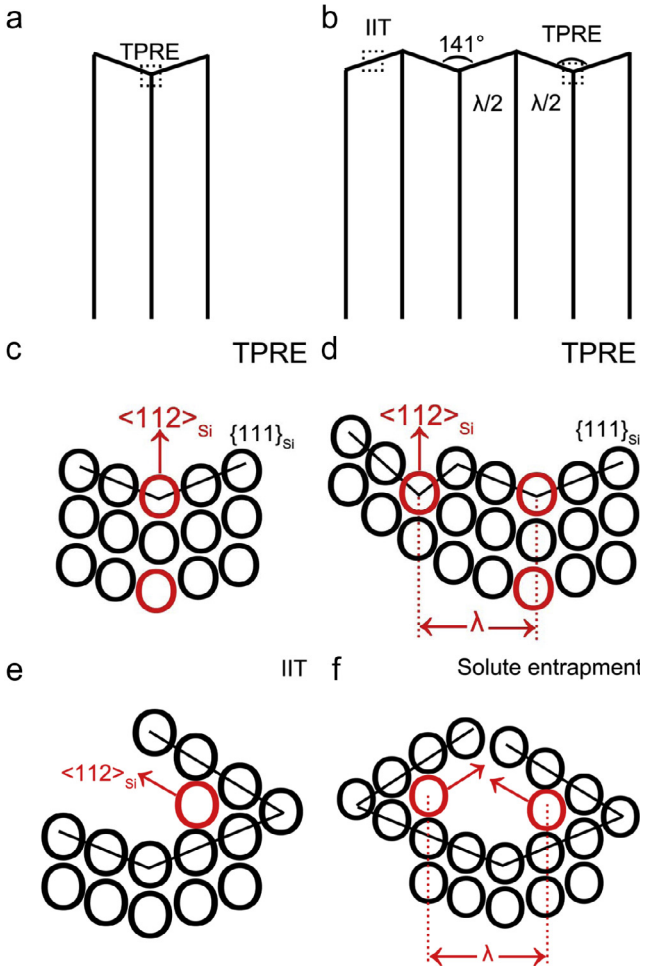

Fig. 15. Schematic representation of the diffusion behaviours of modifying elements ahead of the eutectic Si growth front and its effect on the formation of the parallel Si twinning caused by TPRE or poisoning of TPRE (c, d) and the multiply Si twinning caused by IIT (e, f), as marked in (b). For comparison, natural TPRE is also shown in (a). In the case of TPRE, the adsorption of the modifying elements occurs along the $\langle 1\,1\,2\rangle_{Si}$ growth direction of Si, as shown in (c). A similar adsorption of the modifying elements also occurs on other $\{1\,1\,1\}_{Si}$ growth planes along the $\langle 1\,1\,2\rangle_{Si}$ growth direction of Si, as shown in (d). The diffusion space (λ) is marked in (d). In the case of IIT, the adsorption of the modifying elements occurs at the intersection of two $\{1\,1\,1\}_{Si}$ twins, as shown in (e). A similar adsorption of the modifying elements also occurs at the intersection of two $\{1\,1\,1\}_{Si}$ twins on other $\{1\,1\,1\}_{Si}$ growth planes, as shown in (f). The diffusion space (λ) is also marked in (f).

ahead of Si growth front can be expected to affect the interface energy (γ), diffusion rates in the melt and volume fraction of the Si twins, as observed in Figs. 1, 2, 4, 6 and 7.

The perturbation analysis on the interface stability indicates that the wavelength of the unstable morphology is proportional to the geometric mean of a diffusion length $\left(\frac{D_L}{V}\right)$ and a capillarity length $\left(\frac{\Gamma}{\Delta T_0}\right)$, which has been proposed as [26]:

$$\lambda_i = 2\pi\sqrt{\frac{D_L\Gamma}{V\Delta T_0}} \tag{1}$$

where λ_i is the wavelength of the unstable morphology, defining the critical perturbation which matches both the thermal and solute diffusion field, D_L is the diffusion length, Γ is the capillarity constant (cm, equal to γ/L), γ is the solid–liquid surface free energy/unit area (erg cm^{-2}), L is the latent heat of fusion per unit volume of the pure solvent (erg cm^{-3}), V is the growth velocity and ΔT_0 is the growth restriction, which can be replaced by the expression $mc_0(k-1)/k$.

In the present investigation, the Na addition (50 ppm) appears to promote much more parallel or multiple Si twinning with smaller spaces than the Sr addition (200 ppm), indicating that there is a more significant effect of Na addition than Sr addition on the capillarity length, because the diffusion length can be expected to remain unchanged in the melt-spun condition. On the other hand, the diffusion space (λ) changes when compared with the different cooling rates (melt-spun condition and conventional die-casting). In the melt-spun condition, it is less than 10 nm, as shown in Fig. 3c (for Sr addition) and Fig. 7b (for Na addition), which is much less than that after DSC (more than 100 nm, Fig. 4c and d) and conventional die-casting (more than 200 nm, Fig. 11a). This can be attributed to the fact that in the case of conventional die-casting (Figs. 10–12), the lower cooling rate (lower growth velocity) increases the diffusion length. Thus, the solute adsorption and entrapment of Sr atoms is sufficient during eutectic Si growth. In contrast, in the case of melt-spun condition, the higher cooling rate (higher growth velocity) decreases the diffusion length. The discussion on the diffusion length can be used to interpret our present observation that the presence of the Al_2Si_2Sr phase is within eutectic Si in the case of conventional casting (Figs. 10b and 12b), while no similar large Al_2Si_2Sr phase was observed in the case of melt-spinning. Instead, small Sr-rich clusters were observed. The discussion on diffusion length can also be used to interpret the so-called "quenching modification". The quenching treatment increases the solidification rate, decreases the diffusion length and thus increases the probability to form multiply twinned Si.

In order to further interpret the solute adsorption and entrapment, the diffusivity of modifying elements (i.e. Yb, Na, Sr) in liquid Si (Table 3) is also discussed [27–29]. The diffusivity (D_0) of Yb (solute) in Si (solvent) (2.8×10^{-5} cm^2 s^{-1}) is significantly less than that of Na in Si (2.4×10^{-2} cm^2 s^{-1}), although no data for Sr, to the best of our knowledge, are available. It should be noted that the diffusivity is not temperature-dependent and mainly depends on crystal parameters. The relative diffusion coefficient (D) can be calculated using Eq. (2) [28]:

$$D = D_0 \times \exp\left(\frac{-E}{kT}\right) \tag{2}$$

where D is in m^2 s^{-1}; T is in K; k is the Boltzmann constant, 8.6173324×10^{-5} eV K^{-1}; D_0 is in m^2 s^{-1}; and E, the activation energy, is in eV.

The calculated diffusion coefficients (at 1000 K, ~727 °C) are 4.53×10^{-10} cm^2 s^{-1} (for Yb) and 7.55×10^{-9} cm^2 s^{-1} (for Na). Clearly, Na has a higher diffusion coefficient than Yb, indicating that Na appears to be more chemically active and also to be more likely to diffuse along that Si growth plane. The diffusion coefficient of Sr in Al–5.2Si alloy has been experimentally measured by chronoamperometry to be $(2.00\pm0.10)\times10^{-5}$ cm^2 s^{-1}, which is much higher than the present calculation of Na and Yb [30]. However, it should be pointed out that the diffusion coefficient of Sr was measured in Al–Si–Sr alloy, rather

Table 3. Summary of diffusion parameters in Si [30].

Diffusant	Path	T (°C)	Diffusivity D_0 (cm^2/s)	Activation energies E (eV)
Cu	Bulk	900–1050	0.015	0.86
Fe	Bulk	0–1070	0.0011	0.66
Yb	Bulk	947–1097	2.8×10^{-5}	0.95
Na	Bulk	500–850	2.4×10^{-2}	1.29
Na (with O $3 \times 10^{17}/cm^3$)	Bulk	500–850	1.12×10^{0}	1.64

Table 4. Summary of impurity diffusion in liquid Al and fcc Al [32].

Diffusant	T (°C)	Diffusivity D_0 (cm^2/s)	Activation energies Q (kJ/mol)
Si (in liquid Al)	618–904	0.35×10^{-3}	123.9
Fe (in liquid Al)	700–900	3.7×10^{-3}	16.7
Si (in fcc Al)	–	1.38×10^{-1}	117.6
Fe (in fcc Al)	–	3.62×10^{3}	214.0

than solely within Si. In contrast, a lower diffusion coefficient of Sr in Si at 950 °C was obtained to be $2.00 \times 10^{-17}\ cm^2\ s^{-1}$, highlighting that the diffusion coefficient may be dependent on the measured systems [31]. In the present investigation, the number density of Si twins caused by Na addition (Figs. 6 and 7) is much higher than that caused by Sr addition (Figs. 2 and 3), indicating that the diffusion coefficient of Sr may be less than that of Na under the same solidification conditions. This suggestion can also be used to interpret that Na adsorption may be more likely to occur, promoting Si twinning, whereas Sr may partly segregate out, forming Al_2Si_2Sr phase (Fig. 3b). Only part Sr atoms were adsorbed along the $\langle 1\,1\,2\rangle_{Si}$ growth direction of Si and/or at the intersection of two $\{1\,1\,1\}_{Si}$, promoting Si twinning. The modification effect is thus reduced; even Sr addition (200 ppm) is higher than Na addition (50 ppm). On the other hand, no similar Na-containing phase (i.e. Al_2Si_2Na) was found in the Al–5Si alloys with 50 ppm Na addition, strongly indicating that Na may be mostly dissolved into eutectic Si, resulting into a very strong modification on the eutectic Si.

The diffusivity of the alloying elements (i.e. Si, Fe) in liquid Al and face-centred cubic (fcc) Al is also listed in Table 4 [32]. The diffusivity (D_0) of Fe (solute) in liquid Al or fcc Al (solvent) is significantly higher than that of Si in (solute) in liquid Al or fcc Al (solvent), indicating that Fe atoms are more likely to segregate to liquid Al or fcc Al. However, the activation energies of Fe diffusion in liquid Al ($16.7\ kJ\ mol^{-1}$) is much less than that in fcc Al ($214.0\ kJ\ mol^{-1}$), indicating that the segregation of Fe atoms is easier in liquid Al than in fcc Al, and thereby the Fe-rich phase (i.e. β-Al_5FeSi) was formed in the vicinity of the Si particle, as observed in Fig. 7a. It should be noted that a quantitative analysis of the growth rate and diffusion behaviours of Na, Sr and Yb atoms in liquid Al or fcc Al is impossible due to the unknown growth rate and a lack of relative adsorption data both in the melt-spun condition and in the conventional die-casting condition. Directional solidification experiments and necessary APT and first principles calculations may be still required to further elucidate the diffusion behaviours of the modifying elements and their effects on the interface reaction ahead of the eutectic Si growth. However, it is very clear that the adsorption of the modifying elements ahead of the advancing Si interface should be taken into consideration when discussing any modification mechanisms.

5. Conclusions

1. The solute adsorption of Sr and Na atoms along the $\langle 1\,1\,2\rangle_{Si}$ growth direction of Si and/or at the intersection of Si twins during Si growth was characterised, which can be used to interpret the well-known poisoning of the TPRE and IIT mechanisms, respectively.
2. In contrast, the segregation of Yb atoms is distinctly different from the adsorption of Sr along the $\{1\,1\,1\}_{Si}$ growth planes. No significant Yb-rich cluster was observed at the intersection of Si twins. However, considerable Yb-rich segregation lines were observed along the $\langle 1\,1\,2\rangle_{Si}$ direction, which can be attributed to the solute segregation caused by the few Si twins by natural TPRE. Active poisoning of the TPRE and IIT growth mechanisms were not observed due to the absence of Yb within eutectic Si, in particular at the twin re-entrant edges and/or at the intersection of Si twins.
3. For the first time, the solute entrapment of modifying elements (X) was proposed to interpret the formation of Al_2Si_2X (X, Sr or Yb) phase or X-rich clusters within eutectic Si. Such types of Al_2Si_2X phases or X-rich clusters were further proposed to be an "artefact" caused by the solute entrapment during eutectic Si growth, rather than a "true" modification mechanism.
4. The proposed solute adsorption and entrapment can be used to well interpret the different observations in the cases of different modifying elements, including impurity effects and so-called "quenching modification", thus elucidating the modification of eutectic Si in Al–Si alloys with respect to growth.

Acknowledgment

J.H.L. acknowledges Prof. G. Dehm for his access to the TEM facility at the Erich Schmidt Institute of Materials Science of the Austrian Academy of Sciences.

References

[1] A. Pacz, US Patent No. 1387900, 1921..
[2] Shu-Zu Lu, A. Hellawell, Met. Trans. A 18 (1987) 1721–1733.
[3] R.S. Wanger, Acta Metall. 8 (1960) 57.
[4] R.D. Hamilton, R.G. Seidensticker, J. Appl. Phys. 31 (1960) 1165.
[5] M.G. Day, A. Hellawell, Proc. R. Soc. Lond. A 305 (1968) 473–491.
[6] J.H. Li, S. Suetsugu, Y. Tsunekawa, P. Schumacher, Metall. Mater. Trans. A 44 (2013) 669–681.
[7] K. Nogita, S.D. McDonald, A.K. Dahle, Mater. Trans. 45 (323–32) (2004) 6.
[8] M. Timpel, N. Wanderka, R. Schlesiger, T. Yamamoto, N. Lazarev, D. Isheim, et al., Acta Mater. 60 (2012) 3920–3928.
[9] J.H. Li, M. Zarif, M. Albu, B. McKay, F. Hofer, P. Schumacher, Acta Mater. 72 (2014) 80–98.
[10] J.H. Li, M. Zarif, G. Dehm, P. Schumacher, Philos. Mag. 92 (31) (2012) 3789–3805.
[11] Z.G. Yang, W.X. Du, Senlin Du, S.L. Liu, Acta Metall. Sin. 2 (5) (1989) 316–320.
[12] D. Herlach, P. Galenko, D. Holland-Moritz, Metastable Solids from Undercooled Melts, Elsevier, Amsterdam, 2007.
[13] A. Kar, J. Mazumder, Acta Metall. Mater. 40 (1992) 1873–1881.
[14] H. Assadi, A.L. Greer, ISIJ Int. 35 (1995) 574–579.
[15] H. Assadi, A.L. Greer, Nature 383 (1992) 150–152.
[16] K. Nogita, H. Yasuda, K. Yoshida, K. Uesugi, A. Takeuchi, Y. Suzuki, et al., Scr. Mater. 55 (2006) 787–790.
[17] K. Nogita, H. Yasuda, M. Yoshiya, S.D. McDonald, K. Uesugi, A. Takeuchi, et al., J. Alloys Compd. 489 (415–42) (2010).
[18] M. Zarif, B. McKay, P. Schumacher, Metall. Mater. Trans. A 42 (2011) 1684–1691.
[19] M. Watanabe, D.B. Williams, J. Microsc. 221 (2006) 89–109.
[20] Q.Y. Liu, Q.C. Li, J.R. Zhang, Scr. Metall. 22 (1988) 789–791.
[21] Q.Y. Liu, Q.C. Li, Q.F. Liu, Acta Metall. Mater. 39 (1991) 2497–2502.
[22] K. Kobayashi, P.H. Shingu, R. Ozaki, J. Mater. Sci. 10 (1975) 290–299.
[23] K. Wu, Y. Fujikawa, T. Nagao, Y. Hasegawa, K.S. Nakayama, Q.K. Xue, et al., Phys. Rev. Lett. 91 (2003) 126101.
[24] J.H. Li, J. Barrirero, M. Engstler, F. Mücklich, P. Schumacher, Metall. Mater. Trans. A, Unpublished.
[25] W.M. Wang, X.F. Bian, J.Y. Qin, S.I. Syliusarenko, Metall. Mater. Trans. A 31 (2000) 2000–2163.
[26] W. Kurz, D.J. Fisher, Fundamentals of Solidification, Trans Tech Publications, Zurich, 1998.
[27] H.P. Bonzel, Diffusion in Metals and Alloys, Springer, Berlin, 1990.
[28] M. Kuzmin, P. Laukkannen, R.-L. Vanne, I.J. Väyrynen, Surf. Sci. 515 (2002) 471–482.
[29] D.J. Fisher, Diffusion in Silicon 10 Years of Research, Trans Tech Publications, Zurich, 1997.
[30] Z.G. Yang, W.X. Du, S.L. Du, S.L. Liu, Acta Metall. Sin. 2 (1989) 316–320.
[31] S. Yamamichi, Y. Muramatsu, P.Y. Lesaicherre, H. Ono, Jpn. J. Appl. Phys. 345 (1995) 188–5192.
[32] Y. Du, Y.A. Chang, B.Y. Huang, W.P. Gong, Z.P. Jin, H.H. Xu, et al., Mater. Sci. Eng. A 363 (2003) 140–151.